

From colossal to zero: Controlling the Anomalous Hall Effect in Magnetic Heusler Compounds via Berry Curvature Design

Kaustuv Manna^{1*}, Lukas Muechler^{1,2}, Ting-Hui Kao¹, Rolf Stinshoff¹, Yang Zhang¹, Nitesh Kumar¹, Guido Kreiner¹, Klaus Koepf³, Roberto Car², Jürgen Kübler¹, Gerhard H. Fecher¹, Chandra Shekhar¹, Yan Sun¹, Claudia Felser^{1,†}

¹Max Planck Institute for Chemical Physics of Solids, 01187 Dresden, Germany.

²Department of Chemistry, Princeton University, Princeton, New Jersey 08544, USA.

³IFW Dresden, P.O. Box 270116, 01171 Dresden, Germany

Since the discovery of the anomalous Hall effect (AHE), the anomalous Hall conductivity (AHC) has been thought to be zero in an antiferromagnet, where there is no net magnetization. However, the relation between the intrinsic AHE and the Berry curvature predicts other possibilities, such as a large AHC in non-collinear antiferromagnets. Here we demonstrate that the AHC can be controlled by selectively changing the Berry curvature distribution. Changing the symmetry elements of Heusler magnets switches the Berry curvature and all the associated properties, enabling us to tune the AHC from $0 \text{ } \Omega^{-1}\text{cm}^{-1}$ up to $1600 \text{ } \Omega^{-1}\text{cm}^{-1}$ with an exceptionally high anomalous Hall angle up to 12%. Our study significantly extends the basic understanding of the origin of the intrinsic part of the AHC in magnetic compounds and affords a path towards potential materials with a quantum AHE at higher temperatures. Additionally, it enables the design of new, and switchable magnetic materials with desired magneto-transport properties for potential technological applications.

The Berry curvature distribution in materials determines their topological properties.^{1, 2, 3} For example, in Weyl semimetals, it behaves as a magnetic monopole around the Weyl nodes, and a topological invariant, the Chern number, is assigned to each node.^{4, 5} Additionally, this Berry curvature gives rise to a large intrinsic anomalous Hall effect (AHE) that generally depends on the separation of the Weyl nodes in k space.^{6, 7, 8, 9, 10} The AHE has long been considered the key signature of finite magnetization in ferromagnets or ferrimagnets. For antiferromagnets, the AHE usually vanishes owing to compensation of the magnetic sublattices ($M = 0$). Only recently, it was realized that the *intrinsic* contribution to the AHE of a material derives from its Berry curvature distribution and thus is not directly related to the sample magnetization. For example, the xy component of the intrinsic anomalous Hall conductivity (AHC) is given as,

$$\sigma_{xy}^A(\mu) = e^2 \hbar \left(\frac{1}{2\pi}\right)^3 \int_{\vec{k}} d\vec{k} \sum_{E(n, \vec{k}) < \mu} f(n, \vec{k}, \mu) \Omega_{n,xy}(\vec{k}),$$

where $\Omega_{n,xy}(k)$ is the Berry curvature, $f(n, k)$ is the Fermi–Dirac distribution, and the integral is over the entire Brillouin zone (BZ). In a magnetic material, the Berry curvature transforms according to the symmetries of the magnetic space group and arises from the material's band structure. A necessary condition for a nonzero AHE is the absence of symmetries that reverse the sign of the Berry curvature, e.g., time-reversal symmetry and mirror planes. It is thus possible to control the Berry curvature and intrinsic AHE by suitable manipulations of symmetries and band structures. For example, a large AHC was predicted and recently observed in noncollinear antiferromagnets such as Mn_3Ge or Mn_3Sn , in which the Berry curvature originates from the noncollinear spin structure.^{11, 12, 13}

In magnetic materials, the Berry curvature component along the magnetization direction determines the intrinsic contribution to the AHE. For a set of bands, the Berry curvature depends on how it is connected throughout the BZ.¹⁴ In a magnetic semiconductor without band inversion,

the AHC vanishes, as the occupied valence states can be adiabatically connected to the topologically trivial vacuum (Fig. 1a). In a doped magnetic semiconductor or topologically trivial magnetic metal, the AHC can take small to large values depending on the details of the band structure; it usually follows the density of states (DOS) (Fig. 1b). The energy dependence of the AHC is constrained if there is a trivial band gap close in energy, where the AHC has to vanish. In topological metals, such as Weyl semimetals or nodal line semimetals, the connectivity of the occupied bands is nontrivial owing to the band crossings. While the Berry curvature exhibits a strong peak close to the crossing points, the DOS vanishes, and the AHC peaks sharply in energy, with giant values (Fig. 1c). The inverse relation between the DOS and AHC leads to a large anomalous Hall angle (AHA), unlike the small AHA in regular magnetic metals.

At a symmetry-protected crossing, e.g., in nodal line semimetals, the absence of symmetry leads to a gap of the crossings, and the band structure becomes topologically equivalent to that of a semiconductor (Fig. 1d). We define a band structure as semiconducting in a topological sense, if it can be adiabatically deformed into the band structure of a gapped trivial semiconductor, even if it would be metallic from a transport perspective.

In this paper, we demonstrate these principles theoretically and experimentally and show that the AHC can be selectively tuned from 0 to $1600 \Omega^{-1}\text{cm}^{-1}$ in magnetic Heusler compounds via suitable manipulations of the symmetries and band structures of the materials. Magnetic Heusler compounds are excellent materials for this purpose owing to the diverse possibilities for tuning the electronic and magnetic structure by varying the composition.^{15, 16} The large AHC and high Curie temperature (T_C) allow us to obtain giant AHAs of up to 12% at room temperature.

Ternary Heusler compounds with the formula X_2YZ (where X and Y are transition metals, and Z is a main group element) crystallize in a face-centred cubic lattice with either space group (SG) $Fm\bar{3}m$ (225) (the regular Heusler structure) or SG $F\bar{4}3m$ (216) (the inverse Heusler

structure). In the regular Heusler structure, the X atoms occupy the Wyckoff position $8c$ $(\frac{1}{4}, \frac{1}{4}, \frac{1}{4})$, whereas the Y and Z atoms occupy the Wyckoff positions $4b$ $(\frac{1}{2}, \frac{1}{2}, \frac{1}{2})$ and $4a$ $(0,0,0)$ with Cu_2MnAl ($L2_1$) as the prototype.¹⁷ However, in the inverse Heusler structure, atoms in the $4b$ position replace half of the $8c$ atoms, and the revised atomic arrangement becomes X $[4d$ $(\frac{1}{4}, \frac{1}{4}, \frac{1}{4})]$ X $[4b$ $(\frac{1}{2}, \frac{1}{2}, \frac{1}{2})]$ Y $[4c$ $(\frac{3}{4}, \frac{3}{4}, \frac{3}{4})]$ Z $[4a$ $(0,0,0)]$, with Li_2AgSb as the prototype. The magnetic ground state (ferromagnetic, ferrimagnetic, or antiferromagnetic) of Heusler compounds is controlled by the interatomic distances of the corresponding X and Y atoms and follows the Slater–Pauling rules.¹⁸
¹⁹ Further, T_C generally scales with the sum of the local moments and can reach 1200 K.²⁰

We compare the structures of regular and inverse Heusler compounds in Fig. 2a–2c. The $L2_1$ structure (225) of regular Heusler compounds is symmorphic, and the crystallographic point group is O_h . Upon changing to the inverse Heusler structure, the structure loses inversion symmetry, and the point group reduces to T_d . Fig. 2d–2f show the band structures along the high-symmetry points of three representative compounds. Evidently, the variation in the number of valance electrons (N_V) affects only the position of the Fermi energy E_F within the same symmetry group of compounds, as shown for Co_2MnGa ($N_V = 28$) and Co_2VGa ($N_V = 26$). In both compounds, the spin-up electrons form a topological nodal line, whereas the spin-down electrons are completely gapped. The band structure changes only slightly as the crystal symmetry changes from 225 (Co_2VGa) to 216 (Mn_2CoGa), whereas the total magnetic moment and N_V remain the same. However, this symmetry change converts the topological nodal line semimetal Co_2VGa into the trivial metal Mn_2CoGa (Fig. 1d). Being topologically nontrivial, Co_2VGa and Co_2MnGa should display an AHE with a peak close to the Fermi level (Fig. 1c). In contrast, the AHE of Mn_2CoGa should vanish at an energy close to the Fermi level, as it is topologically equivalent to a regular semiconductor (Fig. 1a).

Fig. 3a and 3c show the M - H hysteresis loops of single crystals of Co_2VGa and Mn_2CoGa , respectively, at temperatures between 2 and 300 K. The saturation magnetizations of the samples correspond to $M_S = 2.0$ and $2.05\mu_B$ at 2 K, respectively, and decrease with increasing temperature. Our measured M_S is in good agreement with the spin magnetic moment predicted by the Slater-Pauling rule, $M_S = (N_V - 24)\mu_B$.^{18, 19} Temperature-dependent magnetization measurements reveal Curie temperatures of 328 K for Co_2VGa and 715 K for Mn_2CoGa [see Fig. S4 in the supplementary information (SI)].

We now discuss the AHE of both compounds. The total Hall resistivity, ρ_{xy} can be expressed as:

$$\rho_{xy} = R_0\mu_0H + \rho_{xy}^{AHE},$$

which is further expanded as $\rho_{xy}^{AHE} = \rho_{xy}^M + \rho_{xy}^T$,

where R_0 is the linear Hall coefficient, ρ_{xy}^{AHE} is the total anomalous Hall contribution, ρ_{xy}^M is the part of the anomalous Hall contribution that usually scales with the magnetization in ferromagnets and ρ_{xy}^T accounts for the topological effects such as spin textures or non-zero Berry curvature.^{12, 13,}

^{21, 22} We calculate the Hall conductivity from the diagonal and off-diagonal components of the resistivity tensor as

$$\sigma_{xy} = \rho_{yx}/(\rho_{xx}^2 + \rho_{yx}^2),$$

where ρ_{xx} is the longitudinal resistivity. All known materials with ferromagnetic or ferrimagnetic ordering that exhibit spontaneous magnetization show an AHE.⁶ Co_2VGa obeys this rule very well, as seen in the summary of magnetotransport measurement in Fig. 3b, with B along the [001] direction. $\sigma_{xy}(B)$ increases linearly for a small applied magnetic field, and anomalous behaviour is observed up to ~ 0.5 T. The Hall resistivity clearly scales with the magnetization at higher fields.

However, at lower B , where the spins are not saturated, ρ_{xy} is expected to have a contribution from the topological component. We estimate the AHC, σ_{xy}^{AHE} , to be $137 \Omega^{-1}\text{cm}^{-1}$ at 2 K, and it gradually decreases at higher temperature to $58 \Omega^{-1}\text{cm}^{-1}$ at 300 K. The Hall coefficient R_0 is calculated from the high field slope of $\rho_{xy}(B)$ as $4.6 \times 10^{-4} \text{ cm}^3/\text{C}$ at 2 K. The sign of R_0 divulges important information about the type of charge carrier involved in transport. The majority charge carriers in Co_2VGa are clearly the hole type in the entire measured temperature range (see Fig. S5 in the SI).

In contrast, Mn_2CoGa shows very different anomalous Hall behaviour. Fig. 3d illustrates the Hall conductivity at various temperatures. Interestingly, σ_{xy} increases linearly with the field, similar to a normal Hall effect. This is an exceptional observation in a metallic magnetic material with a large magnetic moment of $2\mu_B$ and differs markedly with other similar compounds reported in the literature.^{6, 23} The calculated R_0 is $0.035 \text{ cm}^3/\text{C}$ at 2 K for Mn_2CoGa and decreases sharply (by a factor of 10) to $0.0035 \text{ cm}^3/\text{C}$ at 300 K. Consequently, $\sigma_{xy}(B)$ decreases remarkably to a negligible value at 300 K compared to that at 2 K (Fig. 3d). The charge carriers are of the hole type. For all the above measurements, the magnetic field B and current were applied along the [001] and [100] directions, respectively.

As discussed earlier, Mn_2CoGa can be considered as the symmetry-reduced counterpart of Co_2VGa , which has the same N_V . The SG $Fm\bar{3}m$ contains eight symmetry generators, the most important of which are the rotations C_{2y} , C_{2z} , C_{2xy} and the inversion operation I . These together yield M_x , M_y , M_{xy} , and M_{x-y} mirror symmetries ($M_x = C_{2y}C_{2z}I$, $M_y = C_{2y}I$, $M_z = C_{2z}I$, $M_{xy} = C_{2z}I$, and $M_{x-y} = M_zC_{2xy}$). Each mirror defines two-dimensional planes in the BZ (Fig. 2b). For example, M_x generates the mirror planes $(0, k_y, k_z)$ and $(\pm\pi, k_y, k_z)$ via $M_x H(k_x, k_y, k_z) M_x^\dagger = H(-k_x, k_y, k_z)$, on which the eigenstates of the Hamiltonian $H(k)$ can be labeled by a mirror

eigenvalue. A nodal line is formed in the plane when bands of opposite mirror eigenvalues cross. The bands crossings are characterized by an \mathcal{MZ} topological invariant in class A protected by the mirror symmetries.²⁴ Because the mirror planes are related to each other by rotations, a nodal line in one mirror plane implies nodal lines in the other mirror planes. Fig. 2d shows the band structure of Co_2VGa for majority electrons in the $k_z = 0$ plane, where we can see various band crossings with different irreducible representations. In contrast, the SG $F\bar{4}3m$ lacks inversion symmetry; the M_x, M_y, M_z mirror planes are absent, whereas the M_{xy}, M_{x-y} planes are present. Fig. 2f presents the band structure of Mn_2CoGa , which shows gapping of the nodal lines owing to the breaking of inversion symmetry.

We incorporate the effect of spin-orbit coupling (SOC) by considering the spin degrees of freedom. The symmetry of the crystal is reduced depending on the direction of the magnetization, which leads to the gapping of nodal lines and generates Weyl nodes away from E_F .^{14, 25} The rotations and mirror planes orthogonal to the magnetization direction flip the directions of the spins. For example, if we consider magnetization along the \hat{z} direction (as used in the experiment), the mirrors M_x, M_y are no longer allowed symmetry operations of the crystal, whereas M_z remains a symmetry operation. Thus, a gap will appear in the nodal lines in the $k_x = 0, k_y = 0$ plane, unless there is an additional symmetry that can protect a crossing at a certain point. This can, for example, be achieved by the combined time-reversal and rotational symmetries $\mathcal{TC}_{2x}, \mathcal{TC}_{2y}$ and will lead to Weyl nodes derived from the nodal lines.^{14, 25, 26} The absence of nodal lines in inverse Heusler compounds without spin-orbit interaction generally leads to the absence of Weyl points or nodal lines.

Fig. 4a and 4b show the computed spin-resolved DOS for Co_2VGa and Mn_2CoGa , respectively. Co_2VGa is clearly a half-metallic ferromagnet, whereas Mn_2CoGa possesses one

almost-gapped spin channel and one insulating spin channel owing to the absence of inversion symmetry. The closely related compound Mn_2CoAl is a spin-gapless semiconductor in which one spin channel is gapped, whereas the other is semimetallic with a vanishing DOS at the Fermi energy.²⁷

We now discuss the AHC of both compounds (for details of the calculation, see the Methods section). In the limit of weak SOC, the AHC is given as the sum of the conductivities of each spin species, $\sigma_{xy}^A(\mu) = \sigma_{xy}^{\uparrow A}(\mu) + \sigma_{xy}^{\downarrow A}(\mu)$, where μ is the chemical potential. For the half-metallic ferromagnet Co_2VGa , the states around the Fermi level arise only from the majority states, whereas the minority states exhibit a band gap of about 0.2 eV. Thus, the contribution to the AHC of the minority carriers remains constant throughout the band gap energy window (Fig. 4c). Because most of the slightly gapped nodal lines from SOC that generate a large Berry curvature, lie far from the Fermi level (Fig. 2d), the absolute value of the integrated Berry curvature of the spin-up channel is not very large. We calculate an intrinsic AHC of $\sigma_{xy}^A(\mu) = 140 \text{ } \Omega^{-1}\text{cm}^{-1}$ for Co_2VGa , which is consistent with the experiment.

In Mn_2CoGa , however, both spin species possess a finite AHC around the Fermi level (Fig. 4d). The sign of the AHC of the spin-up electrons is opposite to that of the AHC of the spin-down electrons around E_F . Close to E_F , we can approximate $\sigma_{xy}^A(\mu) \approx \sigma_{xy}^{\uparrow A}(\mu) - |\sigma_{xy}^{\downarrow A}(\mu)|$. Therefore, σ_{xy}^A can switch sign depending on which spin channel contributes the most to the overall AHC. At the charge neutrality point, the Berry curvature contribution of the spin-up channel is approximately $74 \text{ } \Omega^{-1}\text{cm}^{-1}$ larger than that of the spin-down channel, resulting in a finite AHC. In our ab initio calculation, the compensation point $\sigma_{xy}^A(\mu) = 0$ lies about 0.1 eV above the Fermi level, which corresponds to approximately 0.1 extra electrons per formula unit. As shown in the SI, our compound is slightly electron-doped, which could explain the discrepancy between theory

and experiment. More importantly, the presence of such a compensation point close to E_F is a general topological property of compounds with an electronic structure topologically equivalent to that of a semiconductor, such as spin-gapless semiconductors. These occur in the inverse Heusler structure owing to breaking of the mirror symmetries if the corresponding full Heusler compound with the same N_V is a half-metallic nodal line semimetal.

We analyse the Berry curvature distribution in k space of the two groups of Heusler compounds to correlate the band structure and corresponding Hall conductivity. As discussed, when Co_2VGa is magnetized along the z direction, the mirrors M_x and M_y are no longer symmetry planes, and a gapless nodal line exists only in the $k_z = 0$ plane. Further reduction of the symmetry could also cause a gap in this nodal line. The band structure of a gapless nodal line contains nonzero Berry curvature around it; however, it is helically distributed in the mirror plane, and the total flux through the mirror plane is zero. Thus, the gapless nodal line in the $k_z = 0$ plane does not contribute to the intrinsic AHC of Co_2VGa . However, the nodal lines in the $k_x = 0$ and $k_y = 0$ planes are gapped by SOC, which forces the Berry curvature to be oriented along the magnetization direction. For example, in the $k_y = 0$ plane (Fig. 4e), the k points around the broken nodal lines are dominated by the negative Ω_{xy} components of the Berry curvature. Because the nodal lines in the mirror planes have strong energy dispersion,^{25,28} only some parts of the nodal lines contribute to the AHC at the fixed Fermi level, resulting in an AHC of $\sim 140 \Omega^{-1}\text{cm}^{-1}$ at E_F . Interestingly, the Berry curvature of Mn_2CoGa contains both positive and negative hot spots and differs markedly from that of Co_2VGa , which is negative in the entire plane. Therefore, during integration of the Berry curvature, hot spots of opposite sign cancel, producing a small AHC value. By doping or temperature effects, one can tune the chemical potential to the topologically required critical point where the positive and negative Berry curvatures are totally cancelled out, yielding *zero* AHC. Interestingly, this is

validated by our experiment, as shown in the inset of Fig. 3d for Mn_2CoGa . As the temperature increases up to 300 K, a nonzero AHE is observed, and $\rho_{xy}(B)$ clearly scales with the sample's magnetization.

To summarize, the interplay of the crystal symmetry with the topological and geometrical properties of the Berry curvature provides a powerful framework to control the AHC.^{10, 29} We condense our findings in Fig. 5, which presents a strategy for tuning the electronic and topological properties of Heusler compounds. In regular Heusler compounds, we find a half-metallic nodal line and Weyl semimetals at different valence electron counts. By suitable chemical substitution, one may destroy the mirror symmetry of the compound (Fig. 5a). The removal of certain mirror symmetries changes the electronic structure of a half-metallic nodal line semimetal into a band structure very close to that of a spin-gapless semiconductor by gapping out the nodal lines; the resulting structure is topologically equivalent to that of a semiconductor. These changes induce corresponding changes in the Berry curvature and thus lead to a small or vanishing AHC. Because of the excellent tunability, one can easily manipulate the chemical potential in Heusler compounds by changing N_V (Fig. 5b). For example, σ_{xy}^A changes from $\sim 140 \text{ } \Omega^{-1}\text{cm}^{-1}$ for Co_2VGa ($N_V = 26$) to $\sim 1600 \text{ } \Omega^{-1}\text{cm}^{-1}$ for Co_2MnGa ($N_V = 28$), which also possesses nodal lines around the Fermi level, although the compounds have different N_V .

Again, keeping the same N_V , when the crystal symmetry is altered from O_h in Co_2VGa to T_d in Mn_2CoGa , σ_{xy}^A decreases to zero (Fig. 5c). The maximum AHA, $\Theta_{AHE} = \Delta\sigma_{xy}^A/\sigma_{xx}$, reaches a giant value of $\sim 12\%$ for Co_2MnGa at room temperature, at which the nodal line is closest to E_F (Fig. 5d). We conjecture that the nodal line dispersion and charge carrier concentration (Fig. 2d and 2e) control the value of Θ_{AHE} , which is why Θ_{AHE} for Co_2VGa is only about 2% (Fig. 5d).

Owing to the extensive tunability of Heusler compounds and the topological nature of our arguments, the compensated AHC should not be unique to Mn_2CoGa . Since all the spin-gapless Heusler semiconductors have similar Berry curvature distributions, the same principle generally applies among all of them, for example, Ti_2CrSi , CoVScSi , and CoFeMnSi . In the SI, we list a series of spin-gapless semiconductor candidate compounds, classified according to the corresponding N_V , that should show a compensated AHC near E_F . Therefore, we can add a new rule to the simple rules of Heusler compounds¹⁷: For each spin-gapless semiconductor, there exists a corresponding half-metallic full Heusler compound with a nodal line in the majority spin channel and Weyl nodes close to E_F with the same N_V , and vice versa. This implies that there should be many more compounds with a large AHC and AHA in the Heusler family. The AHC of the full Heusler compound will generally be large, whereas that of the inverse Heusler compound will be close to zero, as we illustrate for CoFeMnSi and Co_2MnGa , which have $N_V = 28$ (Fig. 5g and 5h, respectively).

Our findings are general and can be extended to other classes of materials with tunable magnetization, as one can control the topology by changing the magnetization and magnetic space group. Thus, our work is relevant to the recent interest in topological classification of magnetic materials, as the topology often constrains the Berry curvature distribution.² By symmetry engineering, a metallic magnet can be converted to a topologically trivial semiconductor with zero AHC. Thus, we demonstrate how the AHC can be tuned from *zero* to a colossal value, independent of the magnetization of the material, for next-generation topo-spintronics applications. Additionally, topological semimetals with a high Curie temperature and large AHA, such as Heusler compounds, are excellent candidate materials for a quantum-confinement-induced quantum AHE in thin films.

Methods

Single crystals of Mn_2CoGa , Co_2VGa , and Co_2MnGa were grown using the Bridgman–Stockbarger crystal growth technique. First, stoichiometric amounts of high-purity metals were premelted in an alumina crucible using induction melting. Then the crushed powder was packed in a custom-designed sharp-edged alumina tube, which was sealed in a tantalum tube. Before crystal growth, the compound’s melting point was determined using differential scanning calorimetry measurement. The samples were heated (to 1150 °C for Mn_2CoGa , 1450 °C for Co_2VGa , and 1250 °C for Co_2MnGa), held there for 10 h to ensure homogeneous mixing of the melt, and then slowly cooled to 750 °C. Single crystallinity was checked by white-beam backscattering Laue X-ray diffraction at room temperature. The crystal structures were analysed with a Bruker D8 VENTURE X-ray diffractometer using Mo-K radiation. Magnetization measurements were performed using a Quantum Design vibrating sample magnetometer (MPMS). The transport properties were characterized by a Quantum Design physical property measurement system (PPMS, ACT option).

The electronic band structure was calculated using density functional theory (DFT) with the localized atomic orbital basis and the full potential as implemented in the full-potential local-orbital (FPLO) code.³⁰ The exchange and correlation energies were considered in the generalized gradient approximation (GGA), following the Perdew-Burke-Ernzerhof parametrization scheme.³¹ To calculate the AHC, we projected the Bloch wave functions into high-symmetry atomic-like Wannier functions, and constructed the tight-binding model Hamiltonian. On the basis of the tight-binding model Hamiltonian, we calculated the AHC using the Kubo formula and clean limit⁷:

$$\sigma_{xy}^z(E_F) = e^2 \hbar \left(\frac{1}{2\pi}\right)^3 \int_{\vec{k}} d\vec{k} \sum_{E(n,\vec{k}) < E_F} f(n,\vec{k}) \Omega_{n,xy}^z(\vec{k})$$

$$\Omega_{n,xy}^z(\vec{k}) = \text{Im} \sum_{n' \neq n} \frac{\langle u(n, \vec{k}) | \hat{v}_x | u(n', \vec{k}) \rangle \langle u(n', \vec{k}) | \hat{v}_y | u(n, \vec{k}) \rangle - (x \leftrightarrow y)}{(E(n, \vec{k}) - E(n', \vec{k}))^2}$$

where $f(n, \vec{k})$ is the Fermi-Dirac distribution, $E(n, \vec{k})$ is the eigenvalue for the n -th eigen states of $|u(n, \vec{k})\rangle$ at the \vec{k} point, and $\hat{v}_{x(y)} = \frac{1}{\hbar} \frac{\partial H(\vec{k})}{\partial k_{x(y)}}$ is the velocity operator. A $201 \times 201 \times 201$ k -grid was used in the integral. We also classified the Berry curvature $\Omega_{n,xy}^z(\vec{k})$ into two species, $\Omega_{n,xy}^{z,\uparrow}(\vec{k})$ and $\Omega_{n,xy}^{z,\downarrow}(\vec{k})$, using the expectation value $\hat{s}_{n,z}(\vec{k})$ of the wavefunction for the given band and k point. The spin-resolved Berry phases $\sigma_{xy}^{z,\uparrow}(E_F)$ and $\sigma_{xy}^{z,\downarrow}(E_F)$ are obtained by taking the integral of $\Omega_{n,xy}^{z,\uparrow}(\vec{k})$ and $\Omega_{n,xy}^{z,\downarrow}(\vec{k})$, respectively, in the entire BZ.

1. Bradlyn B, Elcoro L, Cano J, Vergniory MG, Wang Z, Felser C, *et al.* Topological quantum chemistry. *Nature* 2017, **547**(7663): 298-305.
2. Watanabe H, Po HC, Vishwanath A. Structure and Topology of Band Structures in the 1651 Magnetic Space Groups. *ArXiv e-prints* 2017, **1707**: arXiv:1707.01903.
3. Po HC, Vishwanath A, Watanabe H. Symmetry-based indicators of band topology in the 230 space groups. *Nature Communications* 2017, **8**(1): 50.
4. Bradlyn B, Cano J, Wang Z, Vergniory MG, Felser C, Cava RJ, *et al.* Beyond Dirac and Weyl fermions: Unconventional quasiparticles in conventional crystals. *Science* 2016, **353**(6299).
5. Armitage NP, Mele EJ, Vishwanath A. Weyl and Dirac Semimetals in Three Dimensional Solids. *ArXiv e-prints* 2017, **1705**: arXiv:1705.01111.
6. Nagaosa N, Sinova J, Onoda S, MacDonald AH, Ong NP. Anomalous Hall effect. *Reviews of Modern Physics* 2010, **82**(2): 1539-1592.
7. Xiao D, Chang M-C, Niu Q. Berry phase effects on electronic properties. *Reviews of Modern Physics* 2010, **82**(3): 1959-2007.
8. Burkov AA. Anomalous Hall Effect in Weyl Metals. *Physical Review Letters* 2014, **113**(18): 187202.
9. Kübler J, Felser C. Weyl points in the ferromagnetic Heusler compound Co₂MnAl. *EPL (Europhysics Letters)* 2016, **114**(4): 47005.
10. Kübler J, Felser C. Berry curvature and the anomalous Hall effect in Heusler compounds. *Physical Review B* 2012, **85**(1): 012405.
11. Kübler J, Felser C. Non-collinear antiferromagnets and the anomalous Hall effect. *EPL (Europhysics Letters)* 2014, **108**(6): 67001.
12. Nayak AK, Fischer JE, Sun Y, Yan B, Karel J, Komarek AC, *et al.* Large anomalous Hall effect driven by a nonvanishing Berry curvature in the noncolinear antiferromagnet Mn₃Ge. *Science Advances* 2016, **2**(4).
13. Nakatsuji S, Kiyohara N, Higo T. Large anomalous Hall effect in a non-collinear antiferromagnet at room temperature. *Nature* 2015, **527**(7577): 212-215.

14. Wang Z, Vergniory MG, Kushwaha S, Hirschberger M, Chulkov EV, Ernst A, *et al.* Time-Reversal-Breaking Weyl Fermions in Magnetic Heusler Alloys. *Physical Review Letters* 2016, **117**(23): 236401.
15. Felser C, Fecher GH, Balke B. Spintronics: A Challenge for Materials Science and Solid-State Chemistry. *Angewandte Chemie International Edition* 2007, **46**(5): 668-699.
16. Chadov S, Qi X, Kübler J, Fecher GH, Felser C, Zhang SC. Tunable multifunctional topological insulators in ternary Heusler compounds. *Nat Mater* 2010, **9**(7): 541-545.
17. Graf T, Felser C, Parkin SSP. Simple rules for the understanding of Heusler compounds. *Progress in Solid State Chemistry* 2011, **39**(1): 1-50.
18. Kübler J, Fecher GH, Felser C. Understanding the trend in the Curie temperatures of Co₂-based Heusler compounds: Ab initio calculations. *Physical Review B* 2007, **76**(2): 024414.
19. Galanakis I, Dederichs PH, Papanikolaou N. Slater-Pauling behavior and origin of the half-metallicity of the full-Heusler alloys. *Physical Review B* 2002, **66**(17): 174429.
20. Fecher GH, Kandpal HC, Wurmehl S, Felser C, Schönhense G. Slater-Pauling rule and Curie temperature of Co₂-based Heusler compounds. *Journal of Applied Physics* 2006, **99**(8): 08J106.
21. Neubauer A, Pfleiderer C, Binz B, Rosch A, Ritz R, Niklowitz PG, *et al.* Topological Hall effect in the A phase of MnSi. *Phys Rev Lett* 2009, **102**(18): 186602.
22. Kanazawa N, Onose Y, Arima T, Okuyama D, Ohoyama K, Wakimoto S, *et al.* Large topological Hall effect in a short-period helimagnet MnGe. *Phys Rev Lett* 2011, **106**(15): 156603.
23. Vidal EV, Stryganyuk G, Schneider H, Felser C, Jakob G. Exploring Co₂MnAl Heusler compound for anomalous Hall effect sensors. *Applied Physics Letters* 2011, **99**(13): 132509.
24. Chiu C-K, Schnyder AP. Classification of reflection-symmetry-protected topological semimetals and nodal superconductors. *Physical Review B* 2014, **90**(20): 205136.
25. Chang G, Xu SY, Zheng H, Singh B, Hsu CH, Bian G, *et al.* Room-temperature magnetic topological Weyl fermion and nodal line semimetal states in half-metallic Heusler Co₂TiX (X=Si, Ge, or Sn). *Sci Rep* 2016, **6**: 38839.
26. Chadov S, Wu S-C, Felser C, Galanakis I. Stability of Weyl points in magnetic half-metallic Heusler compounds. *Physical Review B* 2017, **96**(2): 024435.

27. Ouardi S, Fecher GH, Felser C, Kubler J. Realization of spin gapless semiconductors: the Heusler compound Mn₂CoAl. *Phys Rev Lett* 2013, **110**(10): 100401.
28. Yan Z, Bi R, Shen H, Lu L, Zhang S-C, Wang Z. Nodal-link semimetals. *Physical Review B* 2017, **96**(4): 041103.
29. Tung J-C, Guo G-Y. High spin polarization of the anomalous Hall current in Co-based Heusler compounds. *New Journal of Physics* 2013, **15**(3): 033014.
30. Koepnik K, Eschrig H. Full-potential nonorthogonal local-orbital minimum-basis band-structure scheme. *Physical Review B* 1999, **59**(3): 1743-1757.
31. Perdew JP, Burke K, Ernzerhof M. Generalized Gradient Approximation Made Simple. *Physical Review Letters* 1996, **77**(18): 3865-3868.

Supplementary Information is linked to the online version of the paper at www.nature.com/nature.

Acknowledgements

This work was financially supported by the ERC Advanced Grant No. 291472 'Idea Heusler', ERC Advanced Grant No 742068 – TOPMAT, and Deutsche Forschungsgemeinschaft DFG under SFB 1143. T.H.K. acknowledges financial support from the Ministry of Science and Technology, Taiwan, under Grant No. 105-2917-I-110-004. L.M. is grateful for the hospitality of the MPI CPFS, where part of the work was conducted.

Reprints and permissions information is available at www.nature.com/reprints.

Competing financial interests

The authors declare no competing financial interests.

Correspondence

Correspondence and requests for materials should be addressed to K. Manna (email: kaustuvmanna@gmail.com) & C. Felser (email: felser@cpfs.mpg.de).

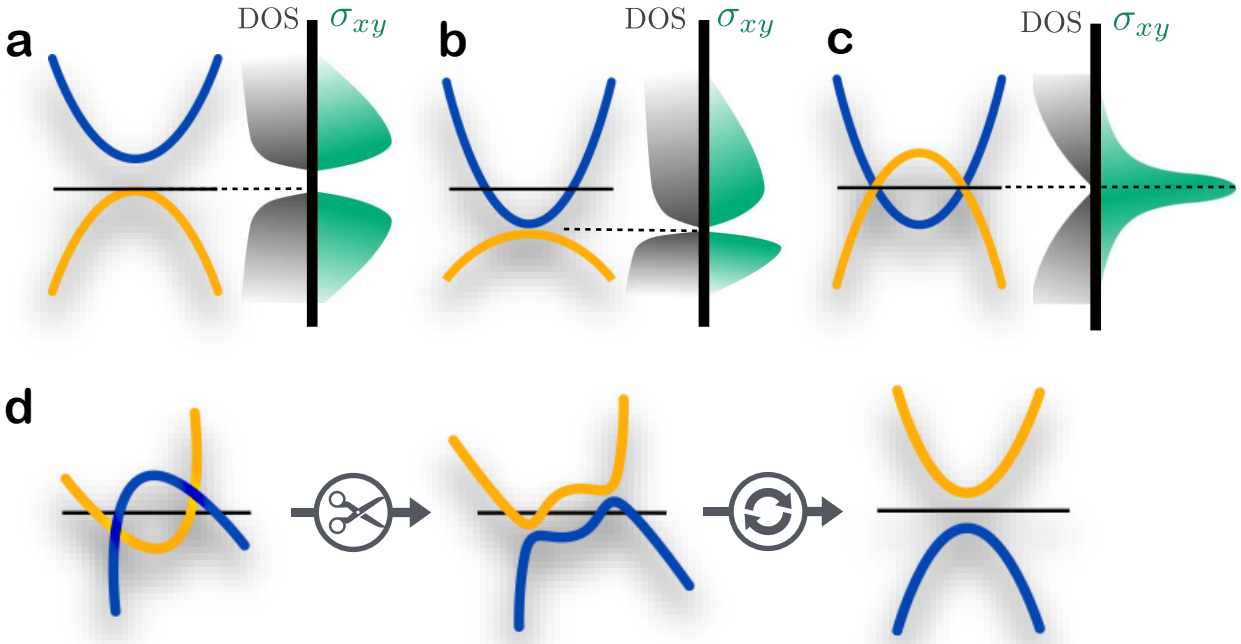


Figure 1: Topologically different band structures and their AHE . Band structure, density of states and AHC of (a) a trivial magnetic semiconductor, (b) a trivial metal, and (c) a topological metal. (d) Change in the topology of a topological metal by gapping out the crossing points via symmetry-breaking or other strong perturbations. The gapped band structure is topologically equivalent to that of a trivial semiconductor.

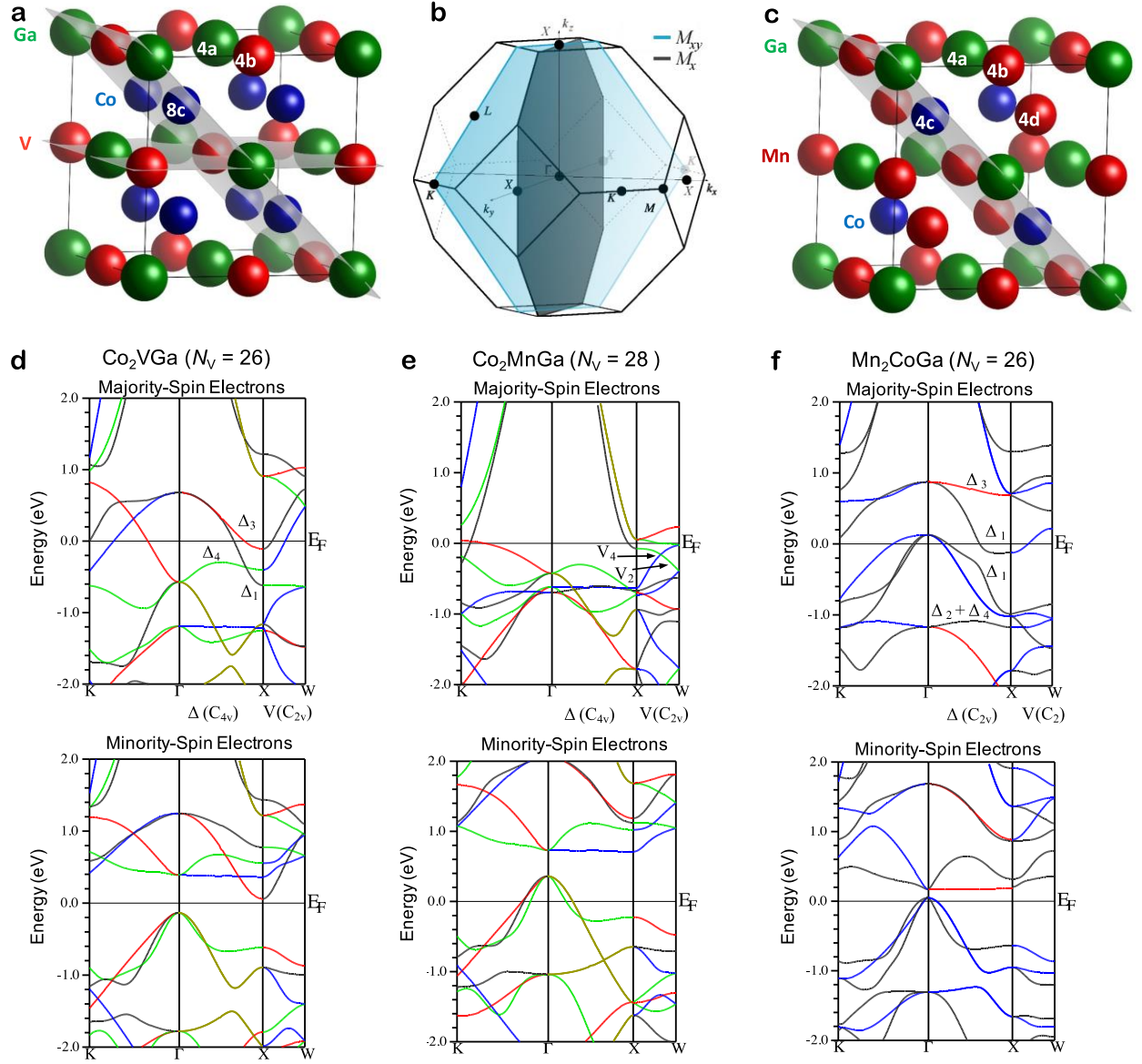


Figure 2: Crystal and electronic band structures of regular and inverse Heusler compounds.

(a) Lattice arrangements and (b) first bulk BZ for the regular Heusler compound Co_2VGa with SG $Fm\bar{3}m$. Corresponding high-symmetry points of the BZ are indicated, along with the allowed mirror symmetries. (c) Lattice arrangements for the inverse Heusler compound Mn_2CoGa with SG $F\bar{4}3m$. The only allowed type of mirror plane is highlighted. Computed band structure of (d) Co_2VGa , (e) Co_2MnGa , and (f) Mn_2CoGa . Colours represent different irreducible representations (denoted by Δ and V) of the little groups at each k .

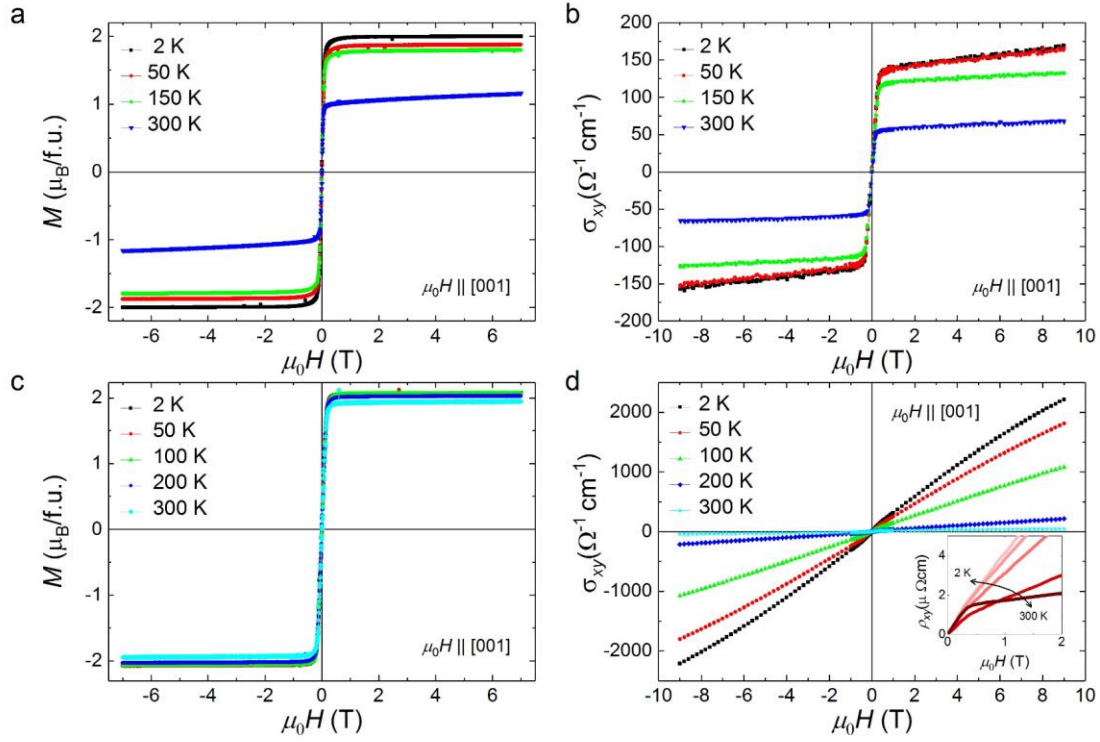


Figure 3: Field dependent Magnetic moment and anomalous Hall conductivity at various temperatures. (a), (c) Magnetic-field-dependent magnetization and (b), (d) corresponding field- and temperature-dependent AHC [$\sigma_{xy}(B)$] of (a), (b) Co₂VGa and (c), (d) Mn₂CoGa single crystals with field along [001] direction. Inset of (d) shows a magnified view of the field-dependent Hall resistivity [$\rho_{xy}(H)$] of Mn₂CoGa at various temperatures from 2 to 300 K in the low-field region.

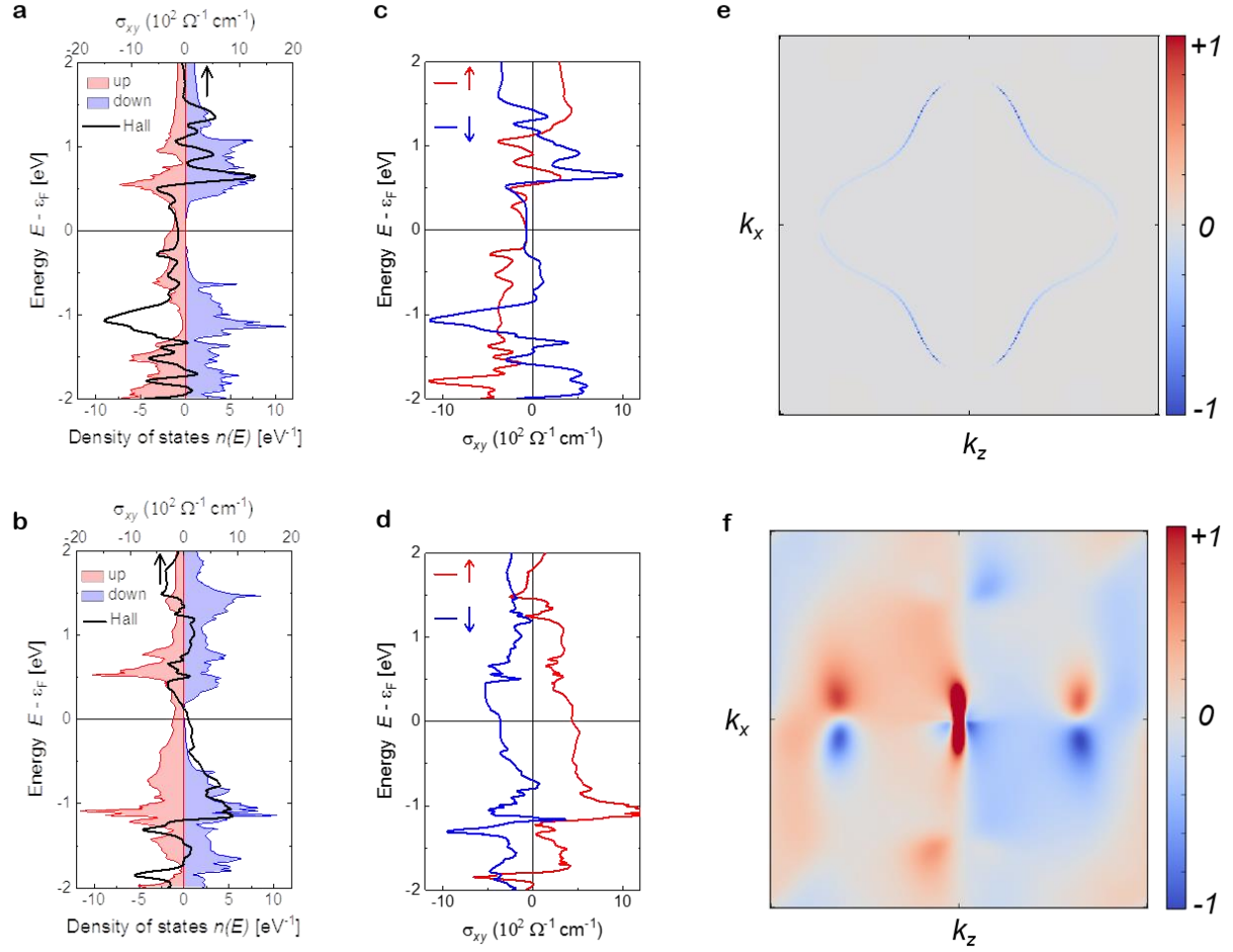


Figure 4: Density of states, Hall and Berry curvature distribution. Computed spin-resolved DOS for (a) Co_2VGa and (b) Mn_2CoGa . Black lines represent the calculated net AHC values. Red and blue represent the DOS for the majority and minority carriers, respectively. Hall contributions in the majority and minority spin channels for (c) Co_2VGa and (d) Mn_2CoGa . Berry curvature of (e) Co_2VGa and (f) Mn_2CoGa at E_F .

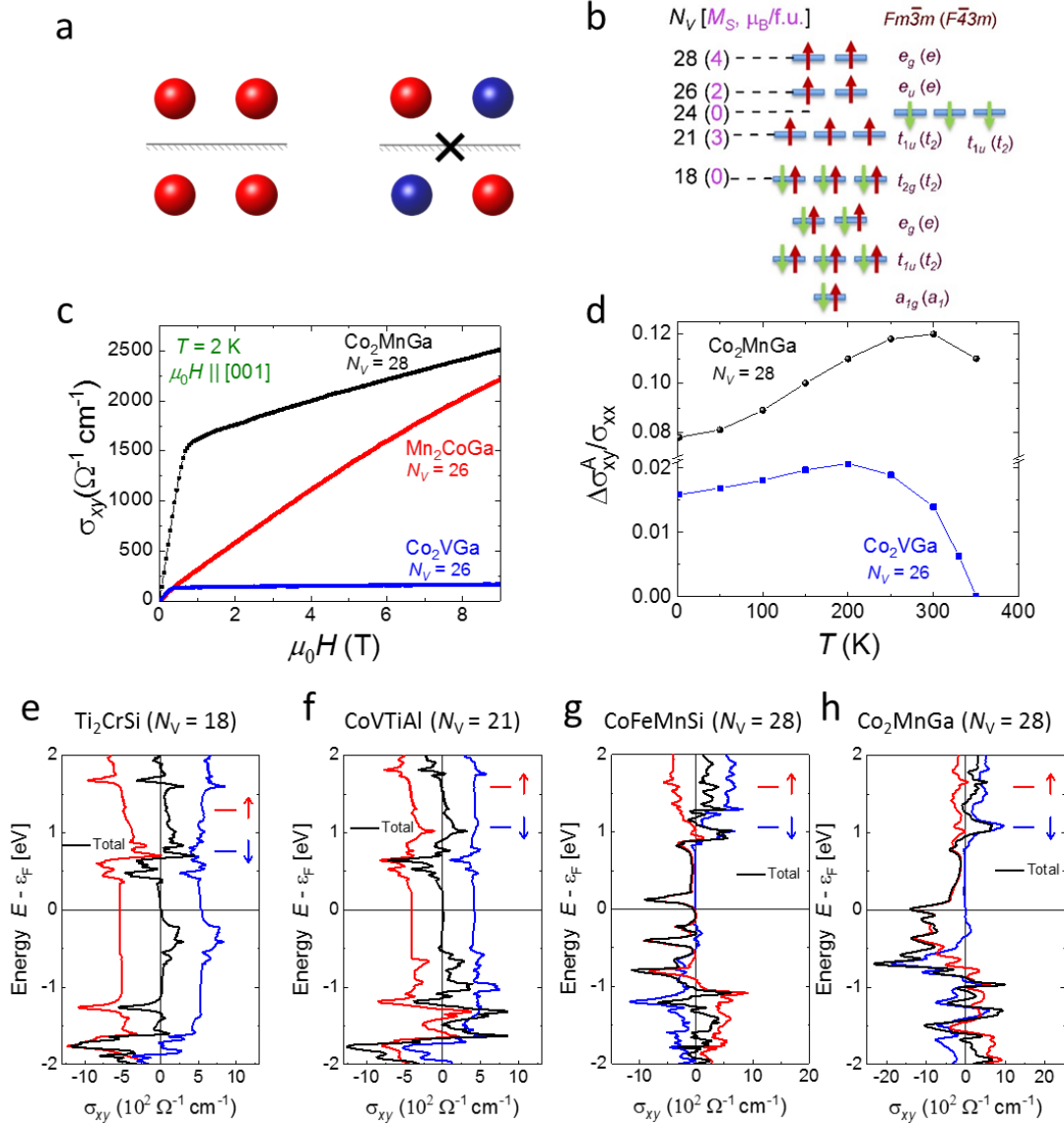


Figure 5: Strategy for tuning the anomalous Hall conductivity. (a) Breaking of mirror symmetry by chemical substitution in the compound. (b) Schematic representation of the distribution of valence electrons in various electronic energy levels for both spin channels and the corresponding net magnetic moment. (c) Experimentally observed Hall conductivity of three magnetic Heusler compounds with various N_V . (d) Temperature dependence of the AHA for two regular Heusler compounds, Co_2MnGa and Co_2VGa . Hall contributions of the majority and minority spin channels and the net AHC for (e) Ti_2CrSi , (f) CoVTiAl , (g) CoFeMnSi , and (h) Co_2MnGa .